A Review on Numerical Simulation of Hydrogen Production from Ammonia Decomposition

Rui Ao [1], Ruihua Lu [2], Guanghui Leng [3], Youran Zhu [2], Fuwu Yan [1] and Qinghua Yu [1,*]

1 Hubei Key Laboratory of Advanced Technology for Automotive Components, Wuhan University of Technology, Wuhan 430070, China
2 Hubei Institute of Aerospace Chemical Technology, Xiangyang 441003, China
3 Wuhan Guohui Intelligent Energy Technology Co., Ltd., Wuhan 430200, China
* Correspondence: qhyu@whut.edu.cn

Abstract: Ammonia (NH_3) is regarded as a promising medium of hydrogen storage, due to its large hydrogen storage density, decent performance on safety and moderate storage conditions. On the user side, NH_3 is generally required to decompose into hydrogen for utilization in fuel cells, and therefore it is vital for the NH_3-based hydrogen storage technology development to study NH_3 decomposition processes and improve the decomposition efficiency. Numerical simulation has become a powerful tool for analyzing the NH_3 decomposition processes since it can provide a revealing insight into the heat and mass transfer phenomena and substantial guidance on further improving the decomposition efficiency. This paper reviews the numerical simulations of NH_3 decomposition in various application scenarios, including NH_3 decomposition in microreactors, coupled combustion chemical reactors, solid oxide fuel cells, and membrane reactors. The models of NH_3 decomposition reactions in various scenarios and the heat and mass transport in the reactor are elaborated. The effects of reactor structure and operating conditions on the performance of NH_3 decomposition reactor are analyzed. It can be found that NH_3 decomposition in microchannel reactors is not limited by heat and mass transfer, and NH_3 conversion can be improved by using membrane reactors under the same conditions. Finally, research prospects and opportunities are proposed in terms of model development and reactor performance improvement for NH_3 decomposition.

Keywords: ammonia decomposition; numerical simulation; heat and mass transfer; hydrogen production

1. Introduction

As a clean and efficient renewable energy, hydrogen energy has attracted wide attention in recent years. Conventional hydrogen production processes, such as autothermal reforming and steam reforming of hydrocarbons and alcohols, will produce polluting gases such as carbon oxides, so it is urgent to find other methods to produce green hydrogen. The single-step decomposition of NH_3 to produce hydrogen proved to be an attractive alternative, because the product gases of NH_3 decomposition are only hydrogen and nitrogen without carbon oxides, and NH_3 has great advantages as a hydrogen storage medium. NH_3 possesses a large hydrogen storage density by weight and volume (17.8 wt%, 108 g/L at 20 °C and 8.6 bar) [1], and zero carbon emissions during the hydrogen production process without any side reactions. NH_3 can be liquefied under relatively mild conditions (0.8 MPa, 298 K), and, therefore, can be stored and transported in liquid form only by pressurizing to 1.0 MPa [2]. The cost of transporting NH_3 is orders of magnitude lower than that of transporting hydrogen. In addition, NH_3 decomposition is relatively easy, which does not need to add oxygen and steam; the explosion limit of NH_3 is narrow, and NH_3 has a pungent odor which is a reliable alarm signal of leakage. Therefore, NH_3 has a high safety performance.

Commercial NH_3 synthesis technology is well established. As its reverse reaction, the NH_3 decomposition has become the focus of interest in recent years. NH_3 decomposition is a mild endothermic reaction ($NH_3 \leftrightharpoons 1/2N_2 + 3/2H_2$ $\Delta H_r = -46.22$ KJ/mol) [3], which yields a high conversion under high temperature and low pressure with the action of catalyst. Experimental, theoretical analysis, and numerical simulation methods can be used to study the reaction characteristics of NH_3 decomposition. Compared to experimental methods, numerical simulation methods are much cheaper to run and provide insight into the reaction behavior inside the reactor. Compared with theoretical analysis, numerical simulation provides more accurate predictions and more specific guidance for design and optimization of reactor configurations. Through experimental methods or theoretical analysis, it is difficult to understand the effects of heat and mass transfer on the NH_3 decomposition process in various reactors. Therefore, it is necessary to use numerical simulation methods such as computational fluid dynamics to predict the behavior inside the reactor.

The accuracy of numerical simulation results is determined by the accuracy of the models. In terms of dimensions of NH_3 decomposition reaction models, there are one-dimensional (1D) models [4], two-dimensional (2D) models [5] and three-dimensional (3D) models [6]. The 1D model is the simplest and requires less computational power. Most studies show that 1D models cannot produce sufficiently accurate simulation results compared with 2D and 3D models. Papadias et al. [7] pointed out that the 1D model can only be used to evaluate the experimental kinetic parameters and to qualitatively evaluate the effects of some design variables on the reactor performance. 1D models can only consider the changes in temperature and concentration along the axial flow direction. This is not in line with actual situations. Most models in the literature are 2D, which provides more accurate predictions compared to 1D models and requires less computational resources than 3D models.2D models assume that variables vary mainly in two directions (e.g., x and y), which are more realistic than 1D models. 3D models are the most realistic models, which can obtain the most accurate results compared with 1D and 2D models and require the most computing resources. With the increase in computing power, 3D models are more and more available, and simulations previously considered impossible can be performed with relatively low computational costs now. In addition, commercial CFD software, such as Fluent, CFX, and COMSOL multiphysics, makes numerical simulation much simpler and more convenient.
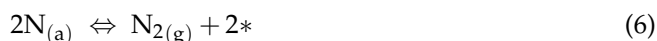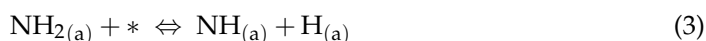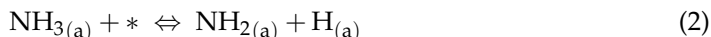
Several reviews have been published on the study of NH_3 decomposition and hydrogen production [8–10]. Lamb et al. [11] reviewed the basic properties of NH_3 decomposition catalysts and briefly discussed techniques for the separation and purification of hydrogen. Chen et al. [12] reviewed the application of ruthenium-based NH_3 decomposition catalysts, focusing on the catalyst carrier materials. In addition, the reaction mechanism NH_3 decomposition under ruthenium-based catalysts in was discussed. Lucentini et al. [13] provide a comprehensive overview of NH_3 decomposition technology, including the state of the art of catalysts, the effectiveness of carriers and promoters, the reaction kinetics of different catalysts, and various reactor technologies. Although these papers all dealt with NH_3 decomposition for hydrogen production, there is no dedicated review in the literature focusing on the application of numerical simulation in various NH_3 decomposition reactors.

In this paper, we review numerical simulations of NH_3 decomposition for hydrogen production in different application scenarios, including microreactors, coupled combustion chemistry reactors, solid oxide fuel cells (SOFC), and membrane reactors. The models they adopted and the factors affecting the reactor performance in various application scenarios are elaborated. This paper provides essential references for the numerical model development and performance improvement of NH_3 decomposition reactors.

This review was carried out based on the database Web of Science. In this database, the following keywords was used to search relevant papers: ammonia decomposition, numerical simulation, microreactor, membrane reactor, combustion reaction and SOFC.

2. Kinetics of NH$_3$ Decomposition Reaction

Reliable chemical reaction kinetics are essential for modeling, and the kinetics of NH$_3$ decomposition over different catalysts have been studied extensively to understand the mechanism of NH$_3$ decomposition and to determine the expression of the reaction rate. NH$_3$ decomposition starts with the adsorption of NH$_3$ molecules on the catalyst surface, followed by dehydrogenation steps and finally the dissociation of hydrogen and nitrogen atoms into H$_2$ and N$_2$ (Equations (1)–(6)) [13].

$$NH_{3(g)} + * \Leftrightarrow NH_{3(a)} \tag{1}$$

$$NH_{3(a)} + * \Leftrightarrow NH_{2(a)} + H_{(a)} \tag{2}$$

$$NH_{2(a)} + * \Leftrightarrow NH_{(a)} + H_{(a)} \tag{3}$$

$$NH_{(a)} + * \Leftrightarrow N_{(a)} + H_{(a)} \tag{4}$$

$$2H_{(a)} \Leftrightarrow H_{2(g)} + 2* \tag{5}$$

$$2N_{(a)} \Leftrightarrow N_{2(g)} + 2* \tag{6}$$

where the subscript (g) represents the gas state; * represents an empty site on the catalyst surfaces; and the subscript (a) represents substance adsorbed on the catalyst surface. The step with the slowest rate among the above 6 steps is called the rate-limiting step. The kinetics of ammonia decomposition are different when adopting different catalysts, and the reaction mechanism depends on the composition, microstructure, and reaction conditions of the catalyst. For example, the nitrogen desorption is identified as the rate-limiting step for Fe and Ni, while for Rh, Pd and Pt, N-H bond breaking is regarded as the rate-limiting step [14]. NH$_3$ decomposition catalysts include noble metals (e.g., ruthenium, palladium, and rhodium), non-noble metals (e.g., nickel and iron), carbides and nitrides, bimetals and poly metals, metal amides and imide, etc [13]. Ruthenium was found to have the highest catalytic activity in decomposing NH$_3$, but it is expensive and difficult to commercialize. Nowadays, commercial catalysts for NH$_3$ decomposition are generally alumina-based nickel because of excellent mechanical properties, thermostability, and lower prices [3].

Many studies have shown that the NH$_3$ decomposition is inhibited by the partial pressure of hydrogen, especially at low temperatures. At low temperatures and high partial pressure of hydrogen, the decomposition rate of NH$_3$ is calculated according to the "Temkin-Pyzhev model" [15]:

$$R_{NH_3} = k_1 \left[\left(\frac{P_{NH_3}^2}{P_{H_2}^3} \right)^\beta - \frac{P_{N_2}}{K_{eq}^2} \left(\frac{P_{H_2}^3}{P_{NH_3}^2} \right)^{1-\beta} \right] \tag{7}$$

where k_1 denotes the rate constant; P_{NH3}, P_{H2}, and P_{N2} are the partial pressures (Pa) of NH$_3$, H$_2$, and N$_2$ (Pa), respectively; β is the fitted parameter in the Temkin–Pyzhev kinetic model; K_{eq} is the thermodynamic equilibrium constant; When the temperature is very high, K_{eq} is very high and the reverse reaction can be ignored. Therefore, the expression is reduced to

$$R_{NH_3} = k_1 \left(\frac{P_{NH_3}^2}{P_{H_2}^3} \right)^\beta \tag{8}$$

$$k_1 = k_0 \exp\left(\frac{-Ea}{RT} \right) \tag{9}$$

where K_0 denotes the pre-exponential factor; Ea denotes the activation energy (J kmol^{-1}); R denotes the universal gas constant (8.3145 J mol^{-1} K^{-1}). K_{eq} can be solved based on the following equation [16]:

$$\log\left(\frac{1}{K_{eq}}\right) = \frac{2250.322}{T} - 0.8534 - 1.5104 \times \log T - 25.8987 \times 10^{-5}T + 14.8961 \times 10^{-8}T^2 \tag{10}$$

At low H_2 partial pressures and high temperatures, the reaction rate is only determined by the NH_3 partial pressure while it is not influenced by the H_2 partial pressure. This model is known as the "Tamaru model" with the following expressions [17,18]:

$$R_{NH_3} = \frac{k_1 K P_{NH_3}}{1 + K P_{NH_3}} \tag{11}$$

$$R_{NH_3} = \frac{k_1 K P_{NH_3}^2}{1 + K P_{NH_3}^2} \tag{12}$$

where K is the adsorption equilibrium constant.

3. Numerical Simulation of NH_3 Decomposition in a Microreactor

Microreactors are miniaturized devices with feature sizes ranging from sub-millimeter to sub-micron. Due to their small scale, they have unique advantages such as large ratio of surface area to volume, efficient mass and heat transfer, and small pressure drops. Common microreactors include microchannel reactors (Figure 1), plate microreactors (Figure 2), and post-microreactors (Figure 3). In microchannel reactors, catalyst is deposited on the stainless-steel channel wall; in plate microreactors, catalyst is deposited on a silicon plate; in post microreactors there are a number of evenly distributed posts, which are coated with catalyst.
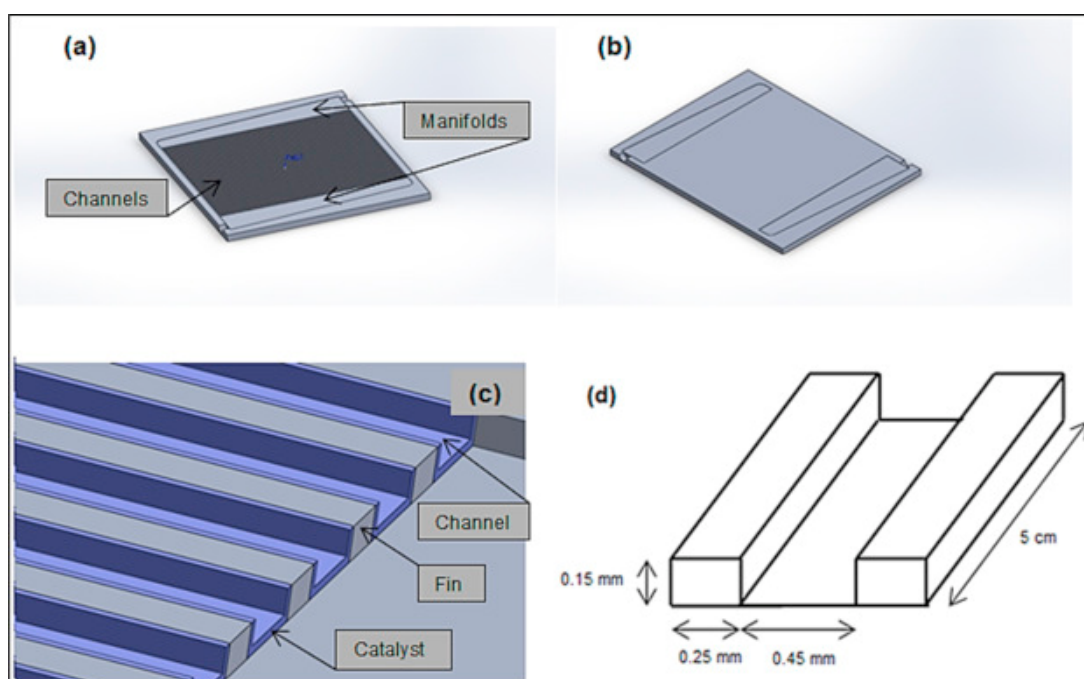

Figure 1. (**a**) 3D schematic of a platelet containing 80 microchannels and fluid distribution manifoldS; (**b**) Platelet with manifold only; (**c**) Enlarged view of the first five microchannels of the platelet (**d**) Sizes of the microchannel without catalyst layer [6].
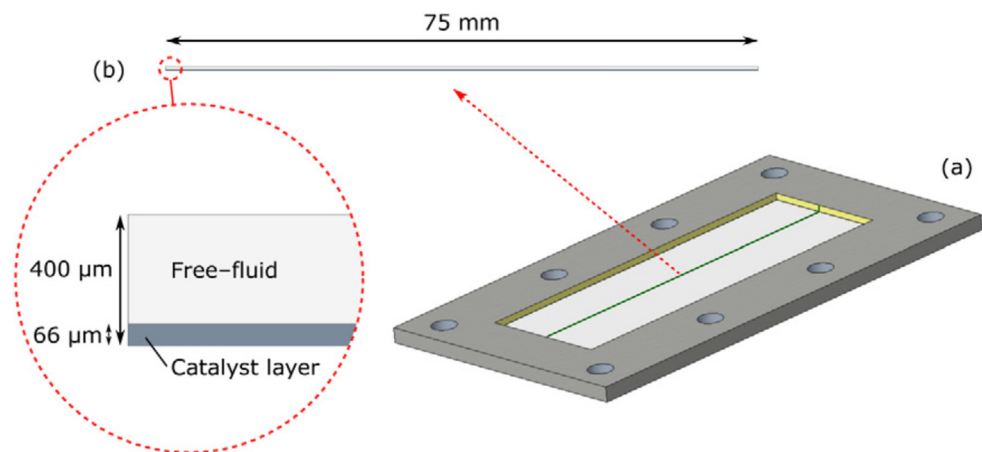
Figure 2. 3D schematic diagram of the plate microreactor (**a**) and distribution of fluid and catalyst (**b**) [19].
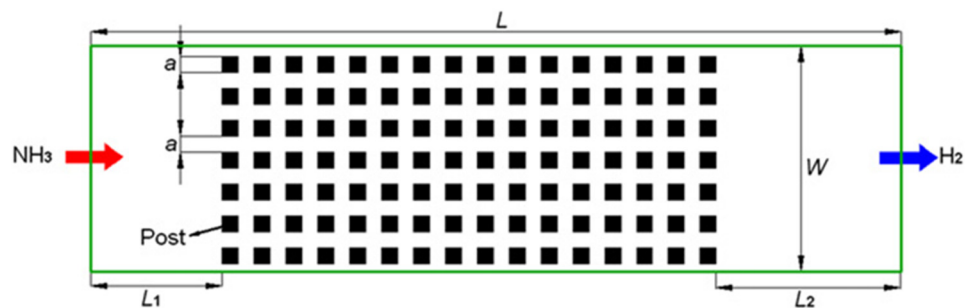

Figure 3. Structures of the post microreactor [20].

3.1. Description of NH$_3$ Decomposition Model in a Microreactor

In a microchannel reactor with a thick catalyst layer as shown in Figure 4a, the reaction occurs within the catalyst layer where molecular diffusion must be taken into account. The microchannel is divided into two computational regions, a free fluid domain located in the middle of the channel and a porous media domain located on the wall representing the catalyst layer [21,22]. If the catalyst layer is thin enough as shown in Figure 4b, the reaction is considered to occur only on the channel wall without any internal molecular diffusion effect. The computational region has only one free fluid domain [5]. Other types of microreactors are treated similarly.
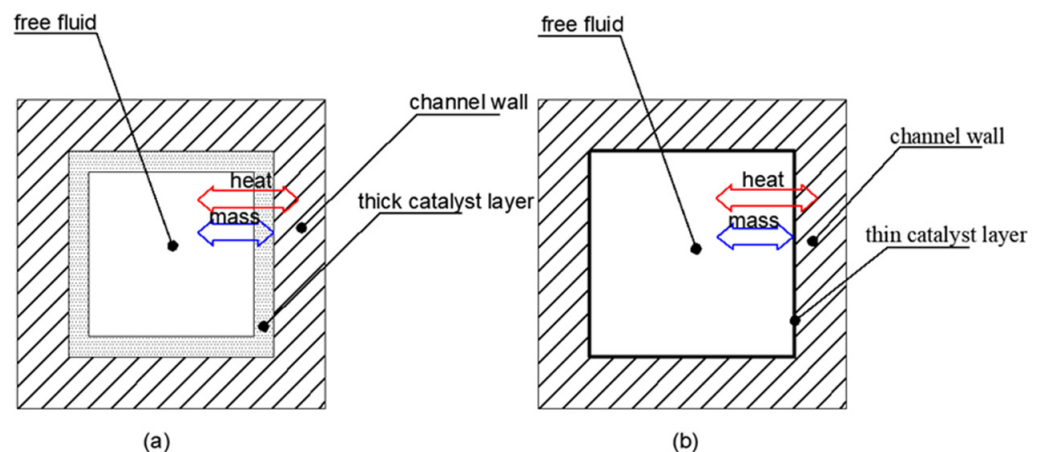

Figure 4. Cross section of microchannel reactor: (**a**) thick catalyst layer; (**b**) thin catalyst layer.

When the NH_3 decomposition reaction occurs, the reactant molecules diffuse from the channel to the surface of the catalyst layer (thin catalyst layer) or further diffuse inside the catalyst layer (thick catalyst layer), and the product gases diffuse along the opposite direction. CFD models are usually used to describe the mass and heat transfer in a reactor over time and space, by solving the conservation equations of mass, momentum, species, and energy, which are as follows:

$$\frac{\partial \rho}{\partial t} + \nabla \cdot (\rho u) = S_m \tag{13}$$

$$\frac{\partial (\rho u)}{\partial t} + \nabla \cdot (uu) = -\nabla p + \nabla \cdot (\nabla \mu u) + S \tag{14}$$

$$\frac{\partial (\rho Y_i)}{\partial t} + \nabla (\rho Y_i u) = \nabla \cdot (\rho D_{ij,eff} \nabla Y_i) + S_{sp} \tag{15}$$

$$\frac{\partial \left(\rho c_p T \right)}{\partial t} + \nabla (\rho c_p u T) = \nabla \cdot (k \nabla T) + S_H \tag{16}$$

where ρ denotes the density (kg m^{-3}); t denotes the time (s); u denotes the velocity (m s^{-1}); S_m is the mass source term (Kg m^{-3}); p denotes the pressure (Pa); μ denotes the viscosity (Pa s); S is the Momentum source term (N m^{-3}); Y_i denotes the mass fraction of species i; $D_{ij,eff}$ denotes the effective diffusion coefficient; S_{sp} is the species source term (kg m^{-3}); c_p denotes the specific heat capacity (J kg^{-1} K^{-1}); T is the temperature (K); k denotes the thermal conductivity (W m^{-1} K^{-1}); S_H denotes the energy source term (W m^{-3}).

Equations (13)–(16) are used in this paper as a general model for NH_3 decomposition reactors. In the literature, most NH_3 decomposition reactor models are derived or simplified from these equations. The Forchheimer equation can be used to calculate the source term in the momentum equation. Thus, in the porous region, the source term is expressed as [23]:

$$S = \frac{\mu u}{B_g} + \frac{C_F}{\sqrt{B_g}} \rho u |u| \tag{17}$$

where B_g is the permeability (m^2) and C_F is the Forchheimer drag coefficient. The energy equation and the species continuity equation of the porous catalyst region include the reaction heat source term and the reaction rate source term because the NH_3 decomposition reaction occurs in these catalyst regions:

$$S_{sp} = \lambda_i R_{NH3} \tag{18}$$

$$S_H = R_{NH3} \Delta H_r \tag{19}$$

where λ_i is the stoichiometric number of species i; R_{NH3} denotes the reaction rate (mol m^{-3} s^{-1}); ΔH_r denotes the reaction enthalpy (J mol^{-1}). D_{ij} represents the binary diffusion coefficient between molecules, which is estimated by Fuller-Schettler-Giddings (FSG) model [24]:

$$D_{ij} = \frac{0.000143 T^{1.75} \left(\frac{1}{M_i} + \frac{1}{M_j} \right)^{\frac{1}{2}}}{P_{atm} \left[\sum v_i^{\frac{1}{3}} + \sum v_j^{\frac{1}{3}} \right]^2} \tag{20}$$

where M_i is the molecular weight of species i (kg mol^{-1}); P_{atm} denotes the atmospheric pressure(atm); v_i are the atomic diffusion volumes (cm^3 mol^{-1}) of species i. The average diffusion coefficient and Knudsen diffusion coefficient of species i in the gas-phase mixture can be expressed as [23,25]:

$$D_i^t = \frac{(1 - X_i)}{\sum j \neq i \frac{X_j}{D_{ij}}} \tag{21}$$

$$D_I^K = \frac{d_p}{3} \sqrt{\frac{8RT}{\pi M_i}} \tag{22}$$

where X_i denotes the Mole fraction of species i and d_p denotes the Mean pore diameter(m). Bosanquet equation is used to calculate the effective diffusion coefficient of porous catalyst region [26]:

$$D_{ij,eff} = \frac{\varepsilon}{\tau} \left(\frac{1}{1/D_i^t + 1/D_{ij}} + \frac{1}{1/D_i^k + 1/D_{ij}} \right) \tag{23}$$

where ε denotes the porosity and τ denotes the tortuosity. The NH_3 conversion is generally calculated using the following formula:

$$X_{NH3} = \frac{n_{in} - n_{out}}{n_{in}} \times 100\% \tag{24}$$

$$X_{NH_3} = \frac{F_{in} - F_{out}}{F_{in}} \times 100\% \tag{25}$$

where n_{in} and n_{out} are the inlet and outlet mole number of NH_3 (mol), respectively; F_{in} and F_{out} are the inlet and outlet molar flow rate of NH_3 (mol s^{-1}).

The density, viscosity, and thermal conductivity of species i depend on temperature. Mass weighted average mixing law is used to calculate the above properties of gas mixtures.

Common assumptions in the literature are as follows:

(1)　The flow is laminar and fully developed;
(2)　Gas types accord with ideal gas behavior;
(3)　Ignoring the homogeneous reaction in the bulk gas phase;
(4)　Negligible pressure drop due to small pressure drop in the reactor;
(5)　The catalyst layer is regarded as an isotropic porous medium;
(6)　Local thermal equilibrium is achieved between the gas mixture and catalyst layer;
(7)　For most channel microreactors, it is generally assumed that the intake distribution manifold distributes the fluid uniformly.

Microreactor modeling and simulation of NH_3 decomposition involve one or two computational domains. The boundary conditions for NH_3 decomposition simulation are as follows:

(1)　The concentration and velocity of gas at the inlet of the channel are specified, and the inlet velocity distribution is even;
(2)　A constant wall temperature is maintained to provide heat for the reaction;
(3)　At the outlet, the pressure is set to atmospheric pressure, and the temperature, velocity and species mass fraction obey Neumann boundary condition (i.e., the normal gradient is zero).
(4)　At all walls, No-slip velocity boundary condition is applied;
(5)　At the interface between the free fluid and catalyst, the velocity, pressure, temperature, and species flux continuity are obeyed.

3.2. Influence Factors on the Performance of NH₃ Decomposition in a Microreactor
3.2.1. Effect of Operating Conditions

As Figure 5 shows, NH_3 conversion increases with the reactor temperature and eventually tends to 100% at 973 K. Chiuta et al. [6] found that when the reaction temperature was 873 K, 80% of NH_3 decomposition was completed within the first 10% of the microchannel. They also stated that the temperature gradient in the microchannel reactor was about 0.03 K

(see Figure 6). For a fixed-bed reactor, Lamb et al. [27] claimed that when the reactor wall temperature was constant at 823 K, the maximum temperature difference inside the reactor reached 70 K. It indicated that the heat transfer performance in a microchannel reactor was better than that in a fixed-bed reactor. For a post microreactor, the temperature gradient is very large (see Figure 7), which is caused by the slow heat transfer between the gas and solid posts and the endothermic reaction, indicating that the heat transfer performance of the post microreactor was far less than that of the microchannel reactor [20]. The large temperature gradient is harmful to the reactor durability. It is essential to strengthen the local heat transfer in the catalytic layer region. The normalized temperature adopted in Figure 7 better shows the temperature change in the reactor relative to the inlet NH_3 temperature caused by the endothermic reaction.
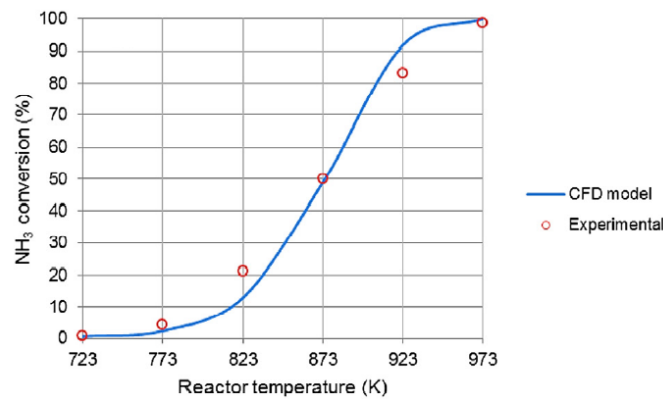

Figure 5. NH_3 conversion versus reactor temperature [28].
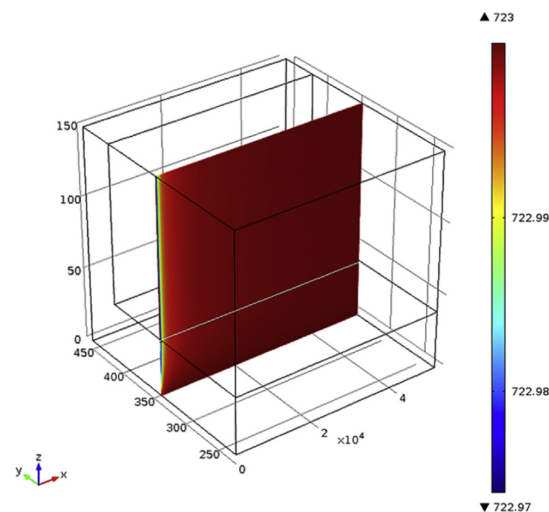

Figure 6. Temperature distribution on the x-z plane of the microchannel reactor at T = 723 K and NH_3 flow rate = 500 Nml min^{-1} [6].
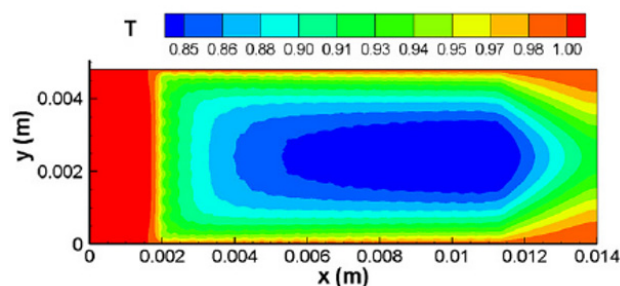

Figure 7. Contours of normalized temperature (T/T_{inlet}) [20].

With the decrease in the ratio of catalyst load to NH_3 molar flow rate (W/F), the contact time between NH_3 gas and catalyst decreases, and therefore NH_3 conversion decreases [6,15]. Chiuta et al. [6] reported that NH_3 conversion was reduced at a much higher NH_3 flow rate (>100 Nml·min^{-1}), but H_2 production was increased.

Pressure can also affect NH_3 decomposition. The decrease in total pressure will promote NH_3 decomposition and increase NH_3 conversion. The presence of hydrogen inhibits NH_3 decomposition, and the NH_3 decomposition rate increases as the hydrogen partial pressure decreases [29,30]. Membrane reactors take advantage of this feature to improve NH_3 conversion, which is discussed further in Section 6.

3.2.2. Effect of Mass Transfer

For characterizing the rates of mass transfer in the porous area and reaction, Maleki et al. [19] defined some characteristic time scales and dimensionless numbers as listed in Table 1. Both Da_{II} and ϕ are less than 1 in their study, which shows that the molecular diffusion time scale is smaller than the chemical reaction time. Figure 8 further depicts kinetic control region and mass transfer control region by Pe and Da_{II}. In the microreactor proposed by Maleki et al. [19], the decomposition reaction occurs in the kinetic control region, which is not restricted by mass transport.

Chiuta et al. [28] also confirmed that the internal diffusion rate was greater than the reaction rate in a microreactor, and a higher NH_3 flow rate would make the diffusion time scale comparable to the reaction time scale. Waghode et al. [5] claimed that the gas diffusion coefficient slightly affected the NH_3 conversion, and the diffusion mechanism was not the main factor affecting the NH_3 conversion in a microreactor. In consequence, internal mass transfer is efficient in a microreactor because of its small size.

Table 1. Definitions and values of characteristic time scales and dimensionless numbers for the microreactor proposed by Maleki et al. [19].

Name	Symbol	Definition	Values
Residence time	t_R	V_R/Q_{in}	0.11–0.56 s
Characteristic reaction time	t_{kR}	$1/k_{app}$	0.012 s
Diffusion time (fluid)	t_D	h^2/D	5.71×10^{-3} s
Effective diffusion time	t_{De}	h_0^2/D_e	9.7×10^{-4} s
Péclet number	Pe	t_D/t_R	0.01–0.051
Damköhler I number	Da_I	t_R/t_{kR}	9.2–46
Damköhler II number	Da_{II}	t_D/t_{kR}	0.47
Thiele modulus	ϕ	$(t_{De}/t_{kR})^{0.5}$	0.28

Where V_R is the volume of the microreactor (m^3); Q_{in} denotes the volumetric flow rate of NH_3 at inlet (m^3 s^{-1}); k_{app} is the apparent reaction rate constant; h is the Microchannel height(m); D is the molecular diffusion coefficient (m^2 s^{-1}); h_0 denotes the porous catalyst layer height (m); D_e denotes the effective diffusion coefficient (m^2 s^{-1}).
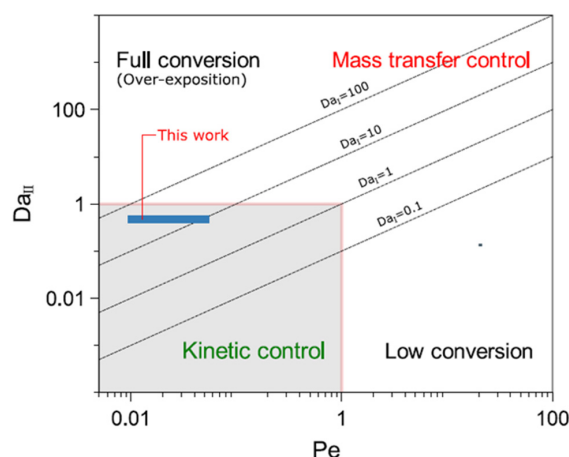

Figure 8. The definitions of kinetic control region and mass transfer region according to Pe and Da_{II} [19].

3.2.3. Effect of the Internal Structure

　　The internal structure of post microreactors can be tailored by adjusting the shapes and arrangements of the internal posts. The post shapes include square, circle, fibrous, etc. The post arrangements include in-line arrangement, staggered arrangement, random arrangement and so on. Among the five post microreactors with different post shapes as shown in Figure 9, the third microfiber reactor outlet has the smallest NH_3 partial pressure, and thus it has the largest NH_3 conversion, but its internal temperature profile is also the most uneven [20]. The highest NH_3 conversion was achieved in the microreactor with a staggered arrangement of catalyst posts, and the worst one was achieved in the microreactor with an in-line arrangement of catalyst posts, while the staggered arrangement led to the largest pressure drop in the reactor. More catalysts fixed at the microreactor wall can obtain higher NH_3 conversion [31]. Under a constant catalyst mass, the NH_3 conversion increases with the post density, whereas the pressure drop also increases [21].
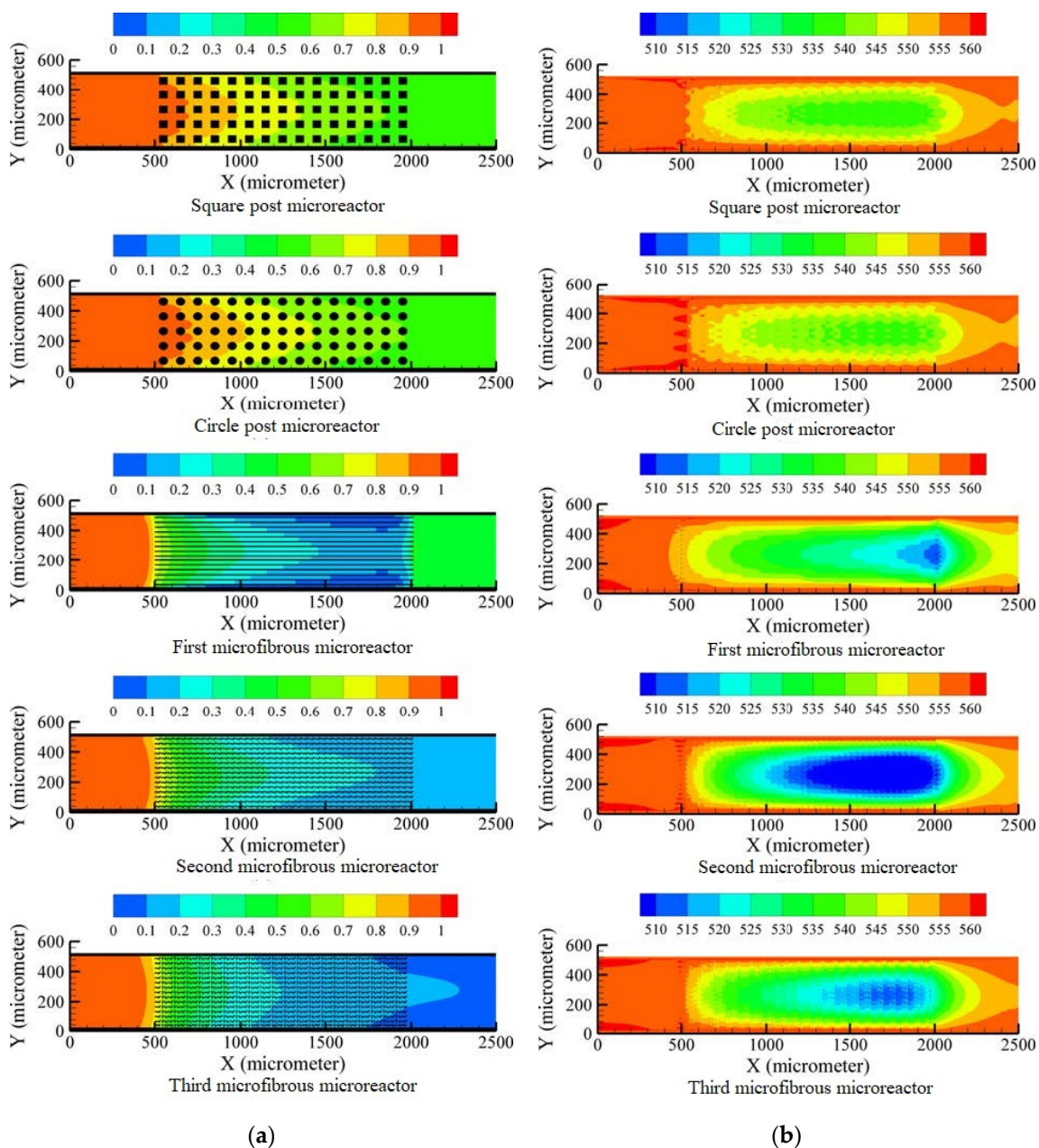

(a)　　　　　　　　　　　　　　　　　　　　　**(b)**

Figure 9. NH_3 partial pressure distributions(atm) (**a**) and Temperature distributions (°C) (**b**) for the five simulated microreactors [31].

The number of channels inside the microreactor also has an impact on the reactor performance. Microreactors with larger hydrogen production are generally multi-channel microreactors [6,32], which may have uneven intake and different temperature distribution. In the existing literature, single-channel modeling is used, which cannot accurately predict the performance of multi-channel. Therefore, the overall model covering all microreactor channels is required to simulate the microreactor more accurately.

3.2.4. Effects of Concentration Jumps, Temperature Jumps, and Velocity Slips

As the characteristic length of a microreactor is close to the molecular average free path, the usual continuity assumption may be broken, and jumps in concentration or temperature can occur at the gas-solid interface. In this state, a continuity equation may still be used, provided that appropriate boundary conditions considering concentration jump, temperature jump and velocity slip are specified. Zade et al. [22] studied the influences of, temperature jump, concentration jump and velocity slip on NH_3 decomposition. The results showed that temperature jump boundary conditions mainly affected the flow and thermal fields, and the discontinuous wall temperature increased NH_3 decomposition; the effects became more obvious with the decrease of channel size; the velocity slip had little influence on the species concentration in the microreactor.

The studies on NH_3 decomposition in microreactors are summarized in Table 2, which provides the adopted catalyst, solving method or tool, nature of work and key points.

Table 2. Summary of numerical simulation of NH_3 decomposition in microreactors.

Catalyst	Solving Method or Tool	Nature of Work	Key Points	Ref
Ni	Discrete using finite element method	Sim	In the microreactor with catalytically active cartridges placed in the center, the overall temperature inside the microreactor did not change significantly, and the effect of heat and mass transfer mechanisms was negligible in the two microreactors studied.	[5]
Ru	FLUENT (version 6.0)	Expt + Sim	The conversion of NH_3 increased sharply with temperature. The effect of post shape on conversion was found to be insignificant and the chemical reaction rate was slower than the lateral mass transfer in the reactor.	[21]
Ni-Pt/Al_2O_3	Lattice Boltzmann method	Expt + Sim	The microfiber reactor had the best NH_3 conversion rate and the highest heat consumption	[31]
Ru/Al_2O_3	COMSOL Multiphysics	Expt + Sim	The microchannel reactor operated under isothermal conditions, and the NH_3 conversion increased with reaction temperature, and this increase was more pronounced in the temperature range of 723–773 K. Heat and mass transfer resistance of the microchannel reactor was quite low.	[6]
CoCeAlO	ANSYS FLUENT 17.2	Expt + Sim	Lateral mass transfer in microchannels was efficient, and thicker catalyst layers ensured higher NH_3 conversion but increased the pressure drop.	[19]
Ni-Pt/Al_2O_3	Lattice Boltzmann method	Expt + Sim	The highest decomposition efficiency of 0.677 was achieved when the posts were staggered; fixing the catalyst near the reactor wall was beneficial to obtain a high reactor performance.	[20]
Ni-Pt/Al_2O_3	COMSOL Multiphysics	Expt + Sim	A porous catalyst layer with a thickness of 40 μm and a channel hydraulic diameter of 225 μm were most desirable for high NH_3 conversion. Mass transfer limitations within the porous catalyst layer and gas phase were inappreciable for the microreactor.	[28]

(Abbreviation: Sim: Simulation work, Expt + Sim: both experimental and simulation work).

4. Numerical Simulation of Coupled Combustion and Decomposition Reactions

The heat required for the NH$_3$ decomposition reaction can be provided by electric heating [33], solar energy [34] and heat release from the combustion chemical reaction. This section discusses the model of a multifunctional microreactor for NH$_3$ decomposition coupled combustion chemical reaction and the factors affecting its performance. The coupled multifunctional reactors can make the device more efficient and compact. There are various forms of thermal coupling, including direct coupling, chronological decoupling coupling, and space separation coupling. Space separation coupling has been extensively studied because it can independently select reaction conditions, catalysts and fuels for endothermic and exothermic reactions [35,36]. The heat transfer coupling between exothermic combustion and endothermic reaction in large devices is well established, but the coupling for small devices is unclear [37]. Therefore, studies on coupled combustion and decomposition reactions are mostly focused on multifunctional microreactors.

4.1. Multifunctional Microreactor Model Description

A multifunctional microreactor comprises of a fuel combustion channel and an NH$_3$ decomposition channel separated by a thermal wall. Three processes are combined in the reactor: fuel combustion process, NH$_3$ decomposition process and heat exchange process of the two channels. As shown in Figure 10, the NH$_3$ gas and fuel flow into two channels with catalyst layers on the wall, and the decomposition and combustion reactions occur in the two channels, respectively.
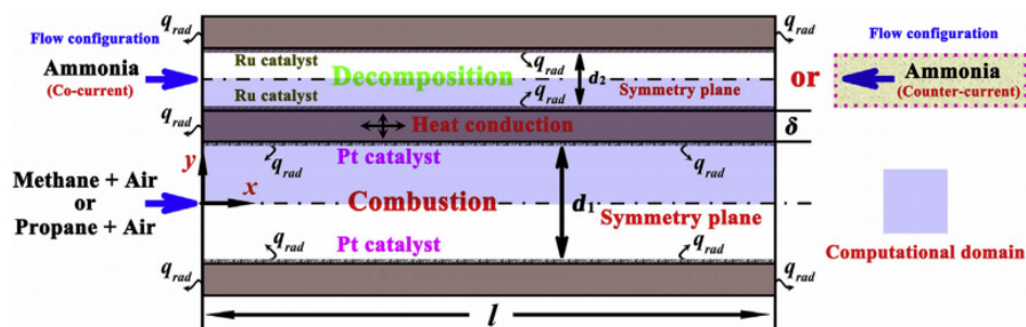

Figure 10. Schematic of a multifunctional microreactor for coupled NH$_3$ decomposition and combustion [37].

The model of the multifunctional microreactor consists of a CFD model for the free fluid domain, a CFD model for the porous domain, an energy conservation equation for the thermal conductivity wall, NH$_3$ decomposition reaction kinetics, and combustion reaction kinetics. The CFD model and the NH$_3$ decomposition reaction kinetics have been introduced in Section 3 and will not be repeated here. The energy conservation equation for a heat-conducting wall is as follows:

$$\nabla \cdot (k_s \nabla T) = 0 \tag{26}$$

where k_s is the thermal conductivity of walls (J·kg^{-1}·K^{-1}).

Commonly used fuels in multifunctional microreactors include methane and propane. The kinetics of the combustion reaction of methane was revealed by Deutschmann et al. [38]. The kinetics of the combustion reaction of propane were proposed by Karagiannidis et al. [39] and by Qin et al. [40].

Regarding the multifunctional microreactor, the common assumptions are the same as those mentioned in Section 3 above, and the boundary conditions often adopted for the multifunctional microreactor include

(1)   At the inlet of the channel, the temperature and flow rate are constant and uniform.
(2)   The reactor outlet is maintained at a fixed pressure.

(3) Neumann boundary condition is applied to the velocity, temperature, and species mass fraction at the outlet.
(4) At all walls a no-slip boundary condition is applied for gas flow.
(5) At all interfaces, the temperature and heat fluxes are continuous.
(6) The device is adiabatic and no heat loss occurs at the sidewalls.

4.2. Homogeneous Combustion and Catalytic Combustion

Fuel combustion is generally classified as homogeneous and catalytic combustion. Homogeneous combustion results in quite high reaction temperatures [32]. Although this is beneficial for NH_3 decomposition [41], the high operating temperature greatly limits the choice of materials leading to NO_x generation and environmental pollution. Compared to homogeneous combustion, catalytic combustion has the advantage of lower operating temperatures, a wider range of conditions for stable operation, a much higher fuel conversion efficiency, and lower NO_x generation [42]. Hence, catalytic combustion is preferred to supply heat for NH_3 decomposition in a multifunctional microreactor.

4.3. Evaluation Index of Multifunctional Microreactor

To evaluate the performance of multifunctional microreactors, reactant breakthrough, material stability, self-sustained operation and maximum power output are defined. Reactant breakthrough denotes the flow rate of fuel corresponding to 99% NH_3 conversion when the fuel is completely transformed in the combustion channel. Material stability denotes the temperature at which the reactor structure materials and catalyst run stably, which is generally considered to be 1500 K. Self-sustained operation denotes the condition in which the reactor can run stably. Maximum output power corresponds to the maximum hydrogen production which is determined by the decomposition rate of NH_3 and the flow rate of fuels. There is usually a contradiction between reactant breakthrough and material stability because low wall temperatures do not allow full conversion of NH_3 [37]. The effects of wall thermal conductivity, NH_3 flow rate, fuel flow rate, and flow configuration on these indexes are discussed below.

4.3.1. Effect of Wall Parameters

Walls have multiple functions in multifunctional microreactors. One is to preheat the combustible mixture to the ignition temperature, and the other is to transfer heat from the combustion reaction to the decomposition reaction. The main parameters of the wall include thermal conductivity and thickness. Reducing the wall thickness produces the same effect as augmenting the wall thermal conductivity [43]. For walls with high thermal conductivity, the internal heat transfer is fast and the wall temperature is close to isothermal. The heat can be quickly transferred upstream of the reactor, making the ignition of the fuel easier. Therefore, it allows a greater range of flow rates for combustible mixtures [37,41].

4.3.2. Effects of Flow Rates of NH_3 and Combustible Mixture

As the NH_3 flow rate increases, the overall wall temperature decreases, which is conducive to the stability of the material, but the NH_3 conversion will decrease [32,41], and the maximum output power will first increase and then decrease. The reason for this trend is that hydrogen production first increases and then decreases [43]. If the flow rate of NH_3 is too large, the heat generated by combustion cannot meet the thermal energy requirement of the NH_3 decomposition process, and the reactor cannot operate self-sustainably [37].

The NH_3 conversion increases with the combustible mixture flow rate, due to the increased heat provided by combustion and the increased reactor temperature. However, the flow rate of the combustible mixture cannot be infinitely increased. The study of Deshmukh et al. [44] shows that too large propane/air flow rate could lead to reactor blowout while too small flow rate could make the reactor fail to operate self-sustainably.

4.3.3. Impact of Flow Configuration

In a multifunctional microreactor, NH_3 and combustible mixture can flow into the channels in the form of co-flow, counter-flow, or cross-flow. Deshmukh et al. [44] pointed out that the counter-flow configuration has greater NH_3 conversion, but larger wall temperature and higher requirements on reactor materials. In a co-flow configuration, the wall temperature is lower and a wider range of materials is available [37]. In a cross-flow configuration, the flow direction of NH_3 is perpendicular to that of fuel/air (see Figure 11). Cross-flow configuration has different operating mechanisms from co-flow and counter-flow, which can significantly reduce NH_3 flow without breaking material stability and is more suitable for low-power equipment [35].
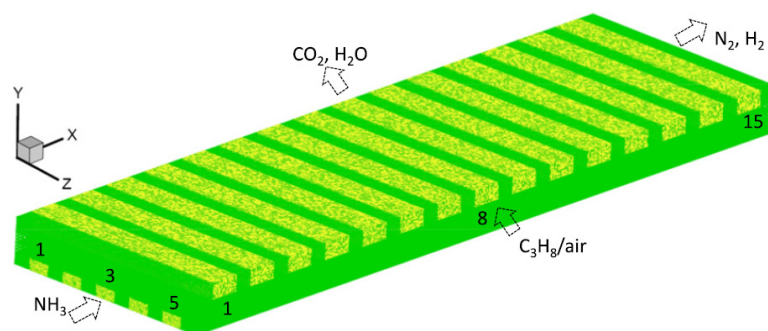

Figure 11. 3D schematic of a cross-flow microreactor [35].

4.3.4. Effect of Other Factors

In addition to the above factors, fuel type and heat loss also affect the performance of multifunctional microreactors. Chen et al. [37] claimed that compared with methane, propane's breakthrough limit occurs at a higher NH_3 flow rate, resulting in greater hydrogen production. Therefore, propane can expand the NH_3 inlet velocity range and thus increase the theoretical Maximum power output. In the literature, researchers mostly used hydrocarbons such as methane and propane as fuels. Their combustion products contain carbon oxides, and hence it is better to use other carb-free fuels such as NH_3. Heat loss in multifunctional microreactors is mainly caused by thermal radiation and convection outside. Since some of the heat generated from fuel combustion is dissipated into the environment via the boundary, a larger flow rate of combustible mixture is required to supply enough heat for NH_3 decomposition [43].

The studies on the numerical simulations of NH_3 decomposition in coupled combustion and decomposition reactors are summarized in Table 3, which provides the adopted fuel, solving method or tool, nature of work and key points.

Table 3. Summary of the numerical simulations of coupled combustion and decomposition reactors.

Fuel	Solving Method or Tool	Nature of Work	Key Points	Ref
Methane and propane	FLUENT Release 6.3 combined with CHEMKIN	Sim	Co-flow structures can lead to lower temperatures and allow for a wider choice of materials. Propane can produce a higher maximum power output than methane. NH_3 decomposition is feasible within a contact time on the order of milliseconds.	[37]
Propane	FLUENT	Sim	Low thermal conductivity walls lead to very high local wall temperatures and significant longitudinal temperature gradients. A higher equipment temperature is obtained at a lower NH_3 flow rate.	[41]
Propane	FLUENT	Sim	Co-flow structure has lower NH_3 conversion, but better reactor stability. A higher NH_3 flow rate reduces the equipment temperature.	[44]

Table 3. *Cont.*

Fuel	Solving Method or Tool	Nature of Work	Key Points	Ref
NH_3	ANSYS CFX	Expt + Sim	As the flow rate of NH_3 for decomposition decreases, the heat consumed by the NH_3 decomposition reaction decreases, resulting in an increase in the steady-state reactor temperature.	[32]
Propane	DASPK software package	Sim	The NH_3 decomposition process is kinetically controlled and the combustion process is controlled by heat transport.	[43]
Propane	FLUENT	Sim	Cross-flow coupled microreactors outperform co-flow microreactors for lower power (lower hydrogen production) applications at a lower NH_3 flow rate.	[35]

(Abbreviation: Sim: Simulation work, Expt + Sim: both experimental and simulation work).

5. Numerical Simulation of NH_3 Decomposition in SOFC

As an efficient carrier of hydrogen, NH_3 can be used in SOFC. SOFC usually adopts a proton-conducting electrolyte (SOFC-H). SOFC-H is taken as an example to illustrate its working principle, as shown in Figure 12. NH_3 is sent into the porous anode while air is sent into the porous cathode. At the anode, NH_3 is catalyzed to decompose into H_2 and N_2. The resulting H_2 undergoes an electrochemical reaction at the anode-electrolyte interface, producing electrons and protons. The electrons from the anode move to the cathode via an external circuit, with electricity generation. The protons travel through the dense electrolyte layer to the cathode-electrolyte interface and react electrochemically with O_2 molecules and electrons to generate H_2O [45].
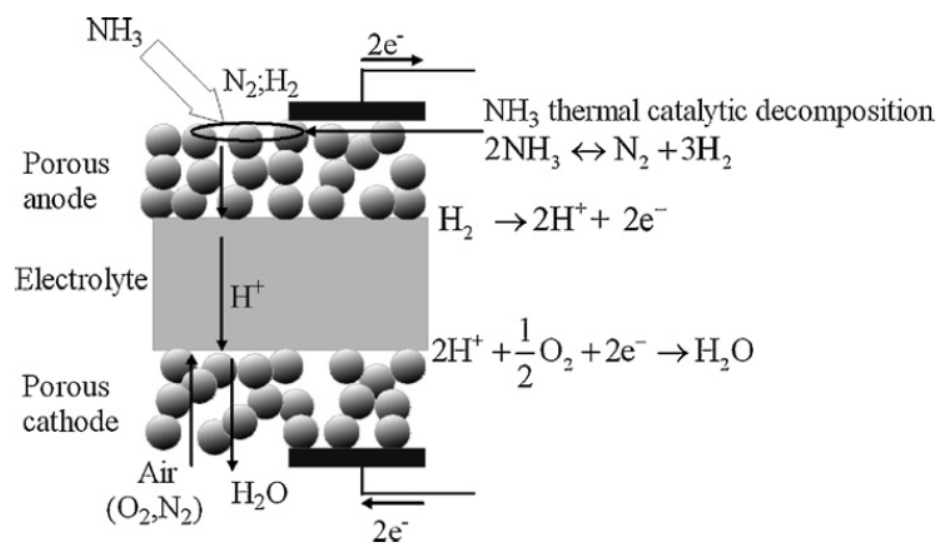

Figure 12. Working principle of SOFC−H with NH_3 as fuel [45].

5.1. Description of SOFC Model

The operating processes of SOFC with NH_3 as fuel include the NH_3 decomposition process, the electrochemical process of SOFC, and the heat and mass transfer process in SOFC. Therefore, SOFC models include the NH_3 decomposition reaction kinetics, electrochemical, and CFD models. The electrochemical model and NH_3 decomposition reaction model are generally associated with the CFD model in the form of source terms. The geometric model of SOFC mainly includes NH_3 and air inflow channels, porous anodes and cathodes, and electrolytes. It can be divided into five calculation regions, including two free fluid domains, two porous media domains, and one solid domain. The kinetic model of the NH_3 decomposition reaction and the CFD model has been introduced in the third section above.

The electrochemical model of SOFC is applied to describe the relationship between current density and electrochemical potential of SOFC, which can be obtained by [46],

$$V = E - \eta_{act,a} - \eta_{act,c} - \eta_{ohmic} \tag{27}$$

$$E = E_0 + \frac{RT}{2F} \ln \left[\frac{P_{H_2}^I \left(P_{O_2}^I\right)^{0.5}}{P_{H_2O}^I} \right] \tag{28}$$

$$E_0 = 1.253 - 0.00024516T \tag{29}$$

where E denotes the equilibrium potential (V), which can be calculated from the Nernst equation [47,48]; $\eta_{act,a}$ and $\eta_{act,c}$ denote the activation overpotentials of the anode and cathode (V), respectively; η_{ohmic} is the ohmic overpotential of the electrolyte (V); E_0 is the equilibrium potential at standard pressure (V); T denotes the local temperature (K); F is the Faraday constant (96,485 C mol^{-1}); P^I is the partial pressure at the electrode-electrolyte interface (Pa). η_{ohmic} can be calculated using Ohm's law [49]:

$$\eta_{ohm} = Jd_e R_e \tag{30}$$

$$J = J_0 \left[\exp\left(\frac{\alpha zF\eta_{act}}{RT} \right) - \exp\left(-\frac{(1-\alpha)zF\eta_{act}}{RT} \right) \right] \tag{31}$$

where J denotes the current density (A m^{-2}); d_e denotes the thickness of the electrolyte (m); J_0 denotes the exchange current density (A m^{-2}); α denotes the symmetry factor; z denotes the number of electrons involved in each reaction. The values of α and z are set to 0.5 and 2 for SOFC, respectively [47,48]. $\eta_{act,a}$ and $\eta_{act,c}$ can be calculated by [44]:

$$\eta_{act,i} = \frac{RT}{F} \sinh^{-1}\left(\frac{J}{2J_{0,i}} \right) = \frac{RT}{F} \ln \left[\frac{J}{2J_{0,i}} + \sqrt{\left(\frac{J}{2J_{0,i}} \right)^2 + 1} \right] \qquad i = a, c \tag{32}$$

The source term S_m in the mass conservation equation (Equation (13)) is non-zero at the electrolyte interface because electrochemical reactions occur in these regions. At the anode-electrolyte and cathode-electrolyte interfaces the source terms are expressed as [46]:

$$S_m = \frac{JM_{H_2O}}{2F\Delta y} - \frac{JM_{H_2}}{2F\Delta y} \tag{33}$$

$$S_m = -\frac{JM_{O_2}}{4F\Delta y} \tag{34}$$

where Δy denotes the control volume width; M_{H2O} and M_{H2} are the molecular weights of H_2O and H_2, respectively (g mol^{-1}).

In the porous anode, the NH_3 decomposition occurs and no electrochemical reaction occurs. The source term in the energy equation (Equation (16)) can be expressed as Equation (20).

In an electrolyte, the energy source term is calculated by [46],

$$S_H = -\frac{JT\Delta S}{2Fd_e} + \frac{J\eta_t}{d_e} \tag{35}$$

where ΔS denotes the entropy change (J K^{-1} mol^{-1}) caused by the reaction [50]; η_t denotes the total overpotential loss (V):

$$\eta_t = V - E \tag{36}$$

In addition to the assumptions in Section 3, there are generally the following assumptions for the SOFC model:

(1)　　The NH_3 decomposition is negligible at locations without a catalyst.
(2)　　The electrochemical reaction involves only hydrogen and oxygen, and the electrochemical oxidation of NH_3 is neglected.
(3)　　At the electrode-electrolyte interface, the ohmic loss is negligible.

In previous studies, the gas composition and flow rate were generally specified at the SOFC gas inlet, and the gas velocity gradient, temperature gradient, and mass fraction gradient were zero at the outlet, while adiabatic conditions were set at outside walls. No-slip boundary conditions were applied at each wall, and continuous conditions of velocity, pressure, temperature and species flux were imposed at all interfaces.

5.2. Effect of Temperature

As the temperature increases, the conversion of NH_3 in SOFC increases, and the concentration overpotential and effective diffusion coefficients of the anode and cathode of SOFC increase [49]. Ni et al. [45] claimed that when SOFC was operated at high temperatures (1073 K or 873 K), NH_3 could totally decompose into H_2 before reaching the electrochemical reaction region, while SOFC at lower temperatures (773 K or 673 K), only part of NH_3 can decompose into H_2 before reaching the electrochemical reaction region. With an increase of the SOFC temperature, both the Nernst potential and current density of SOFC increase [46], due to the increase of hydrogen generated from NH_3.

5.3. Temperature Distribution in the SOFC

There are heat production by an electrochemical reaction, heat production by irreversible overpotential loss, and heat consumption by thermal decomposition of NH_3 in SOFC. Studies [51] have shown that the heat required by the thermal decomposition of NH_3 is larger than the heat produced by electrochemical reaction and overpotential loss. Along the flow direction of NH_3, the temperature decreases as shown in Figure 13 [46].
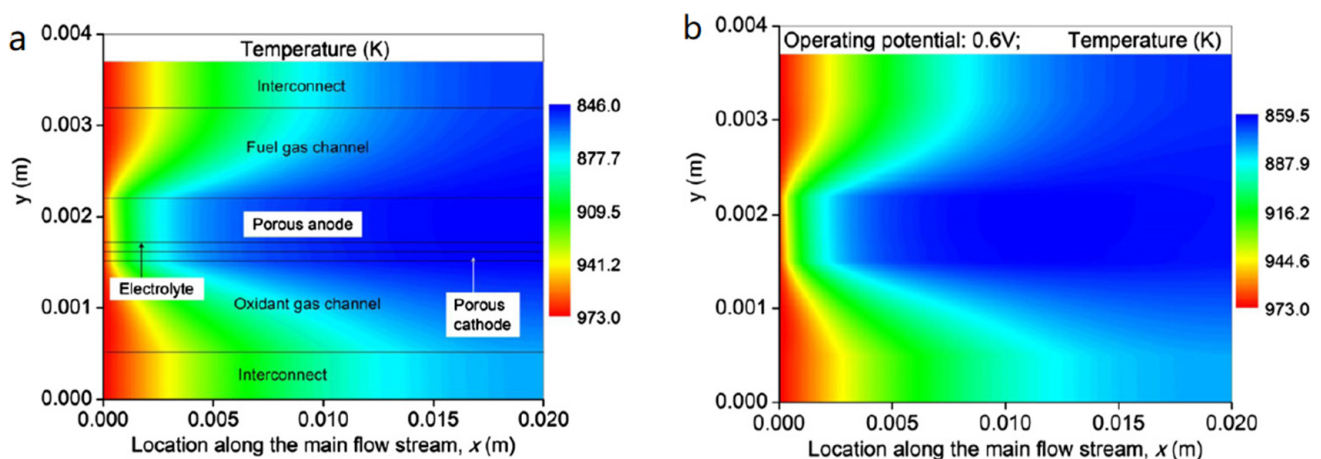

Figure 13. Temperature distribution in SOFC at an inlet temperature of 973 K with an operating potential: (**a**) 0.8 V; (**b**) 0.6 V [46].

5.4. Effect of Operating Potential

Ni et al. [46] stated that as the operating potential decreased from 0.8 V to 0.6 V, the maximum temperature difference in SOFC decreased from approximately 127 K to approximately 115 K (see Figure 13); the current density was elevated from 5860.4 A·m^{-2} to 9160.1 A·m^{-2}; the power density increased from 4688.3 W·m^{-2} to 5496.1 W·m^{-2}. As the operating potential was further reduced to 0.3 V, the maximum temperature difference decreases to about 97 K; the current density further increased to 14,232.4 A m^{-2}, whereas the power density greatly decreases to 4269.7 W m^{-2}. This indicates that lowering the operating potential decreases the temperature difference in SOFC, but too small operating potential leads to a decrease in output power.

6. Numerical Simulation of NH$_3$ Decomposition in the Membrane Reactor

A membrane reactor is also a multifunctional reactor in nature, which integrates NH$_3$ decomposition and hydrogen purification into a single unit. Many studies have proved that the produced hydrogen will inhibit the further NH$_3$ decomposition, and expelling the produced hydrogen from the system can increase the partial pressure of NH$_3$ and promote the reaction towards the generation of hydrogen, thus improving the conversion of NH$_3$. So far, in addition to the palladium membrane, there are silica, zeolite, and carbon membranes used in the membrane reactor. Each membrane material has defects: Palladium is prone to failure under the action of H$_2$S and CO; the permeability of silica is low for H$_2$; zeolite and carbon membranes have low H$_2$ selectivity [52]. Since palladium film is only permeable to H$_2$ and has a high permeability, most studies still use palladium film.

6.1. Model Description of NH$_3$ Decomposition in a Membrane Reactor

As shown in Figure 14, a typical membrane reactor consists of tube side, palladium membrane, and shell side. The catalyst particles are installed in the whole tube side, and the preheated gaseous NH$_3$ enters the reactor through the inlet of the tube side, where it decomposes into H$_2$ and N$_2$. Owing to the H$_2$ pressure difference between the tube side and shell side, part of H$_2$ selectively penetrates the membrane and travels to the shell side. The residual H$_2$, remaining unconverted NH$_3$ and N$_2$ flow out of the tube side via the outlet. On the shell side scavenging or vacuuming is generally adopted to reduce the hydrogen partial pressure, while on the tube side the H$_2$ partial pressure is increased by pressurization.
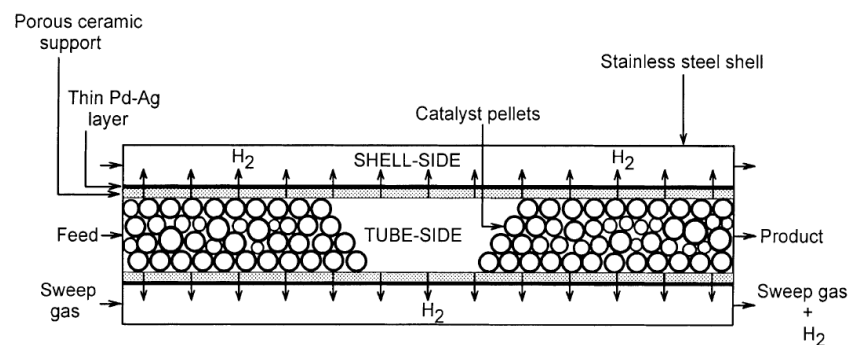

Figure 14. Schematic of the co-flow membrane reactor [53].

The model of the membrane reactor involves the CFD model and the hydrogen permeation equation for the palladium membrane. It consists of three computational domains: the shell-side free fluid domain, the tube-side porous domain, and the palladium membrane porous domain. The CFD models for the free-fluid and porous domains are described in Section 3 above. Regarding the hydrogen permeation equation for palladium membranes, the Fick-Sieverts law is generally used [54,55]:

$$Q_H = Q_0 (P_{H,t}^{1/2} - P_{H,s}^{1/2}) \left(\frac{A}{\delta} \right) \tag{37}$$

Q_0 is the hydrogen permeability constant (mol/(m·s·Pa$^{0.5}$)); A denotes the membrane area available for permeation (m^2); δ denotes the membrane thickness. Q_0 obeys Arrhenius law:

$$Q_0 = k_a \exp \left(\frac{E_H}{RT} \right) \tag{38}$$

where k_a is the pre-exponential constant (mol/(m·s·Pa$^{0.5}$)), and E_H is the activation energy for membrane permeability (J/mol).

In addition to some simplifications proposed in Section 3, the following simplifications are usually made during the modeling of membrane reactors for NH$_3$ decomposition:

(1) The membrane is permeable only to hydrogen;
(2) There is no axial diffusion in the membrane;
(3) NH_3 and N_2 do not cause membrane surface poisoning and lead to membrane performance degradation.

6.2. Influencing Factors of Membrane Reactor Performance

The evaluation indexes of membrane reactor performance mainly include NH_3 conversion, hydrogen production, and hydrogen purity, which are affected by temperature, sweep gas flow rate, W/F, membrane thickness, etc. As the membrane reactor temperature or sweep gas flow rate was elevated, the NH_3 conversion and hydrogen production were significantly improved [56,57]. The decrease of W/F reduced the contact time between NH_3 and the catalyst, causing part of NH_3 to be discharged from the reactor without time to decompose, which is not conducive to the NH_3 conversion [58]. The decrease in membrane thickness led to a decrease of hydrogen permeability resistance and an increase of hydrogen permeability. Therefore, the increase in membrane thickness is conducive to the improvement of NH_3 conversion [30]. H_2 purity was mainly dependent on the membrane properties and slightly affected by W/F, temperature and pressure, under whose wide ranges H_2 purity exceeds 99.2% [58]. For porous silica membranes that allow N_2 and NH_3 to permeate with H_2, hydrogen purity decreased due to the infiltration of N_2 and NH_3 [59].

6.3. Rate-Limiting Step of Hydrogen Permeation in Membrane Reactor

Figure 15 displays the dependence of transverse Peclet (Pe_t) number and Λ number on gas hourly space velocity [58]. Pe_t and Λ are calculated by Equations (39) and (40), respectively. When the gas hourly space velocity was greater than 300 scc/hr/g cat, the value of Pe_t was greater than 1 (see Figure 15a), indicating that radial diffusion played a dominating role in the reactor behavior. From Figure 15b, it can be found that the radial diffusion of the gas phase was significantly slower than the permeation through the membrane. The reason for this phenomenon was the concentration polarization of the membrane surface. Their study demonstrated that radial diffusion was a rate-limiting step in membrane reactors.

$$Pe_t = \frac{\tau_d}{\tau_f} = Pe_{H_2r}\frac{(R_i - r_m)^2}{R^2} \tag{39}$$

$$\Lambda = \frac{\tau_d}{\tau_p} = \theta\frac{(R_i - r_m)^2}{R}\frac{S_{me}}{V_r} \tag{40}$$

where τ_d is the characteristic radial diffusion time (s); τ_f is the characteristic flow time (s); Pe_{H2r} is the modified transverse Peclet number for H_2; R_i is the inner radius of packed bed (m); r_m is the outer radius of Pd fiber(m); τ_p is the characteristic permeation time (s); θ is the non-dimensional parameter [58]; S_{me} is the membrane surface area (m^2); V_r is the reactor volume (m^3).
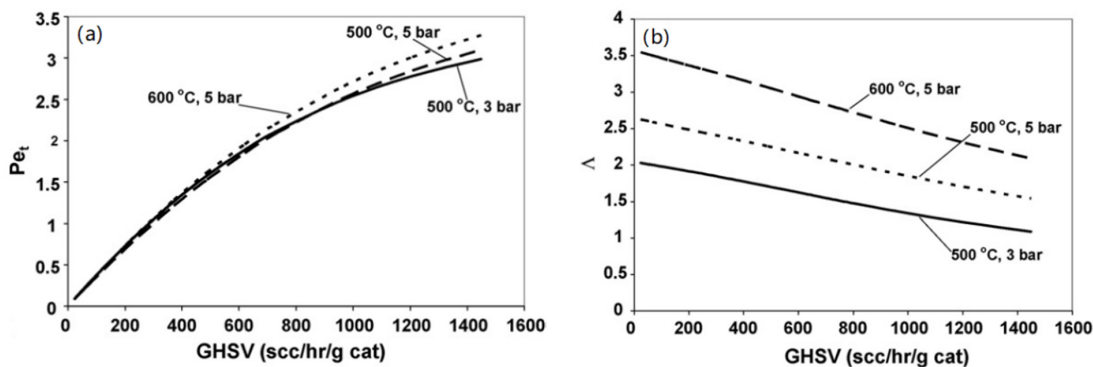

Figure 15. Dependence of Pe_t number (**a**) and Λ number (**b**) on GHSV under different working conditions [58]. GHSV denotes the gas hourly space velocity; cat denotes the catalyst.

6.4. Improvement of Membrane Reactor Performance

To reduce the limitation of radial diffusion in membrane reactors, Zhang et al. [60] developed a catalytic membrane reactor (CMR). As Figure 16 shows, the catalyst layer is adjacent to the membrane in the CMR and H_2 is released directly near the permeable membrane during decomposition while the catalyst pellets are dispersed in the channel of the packed-bed membrane reactors (PBMR). Therefore, the diffusion scale of H_2 in the CMR is micron-sized while it is millimeter-sized in the PBMR. As a result, the CMR exhibited less amount of catalyst, lower operating temperatures and higher H_2 yield than the PBMR.
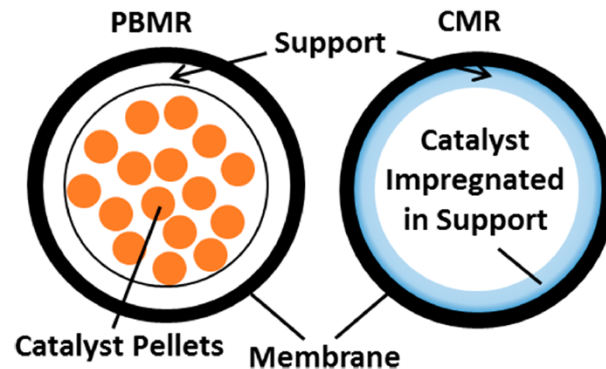

Figure 16. Comparison of cross-sections between a PBMR and a CMR [60].

Abashar et al. [53,61] developed two types of membrane reactor structures to further improve the NH_3 conversion. The first one [53] is a structured catalyst bed membrane reactor (see Figure 17a). In the membrane reactor, there are two catalysts, one for NH_3 decomposition and the other for methanation, which are arranged in a mixed or layered structure in the membrane reactor. Methanation as an auxiliary reaction is designed to remove hydrogen from the reactor, and the results show that NH_3 can be completely decomposed at low temperatures within the effective length range in this type of membrane reactor. The second type [61] is a fixed-bed membrane reactor (FBMR) with distributed injection feed (see Figure 17b). In this membrane reactor, NH_3 injection points are uniformly arranged on the shell side, and NH_3 can be fed into the membrane reactor through the injection points beside the inlet. They have verified that this design could greatly diminish the reactor length. The conversion of NH_3 was increased first and then decreased with the increase in the injection point number. When the number of injection points was 5, the reactor performance was optimum, which could significantly shorten the reactor length by 75.0%, and the NH_3 conversion rate could reach 100.0%.
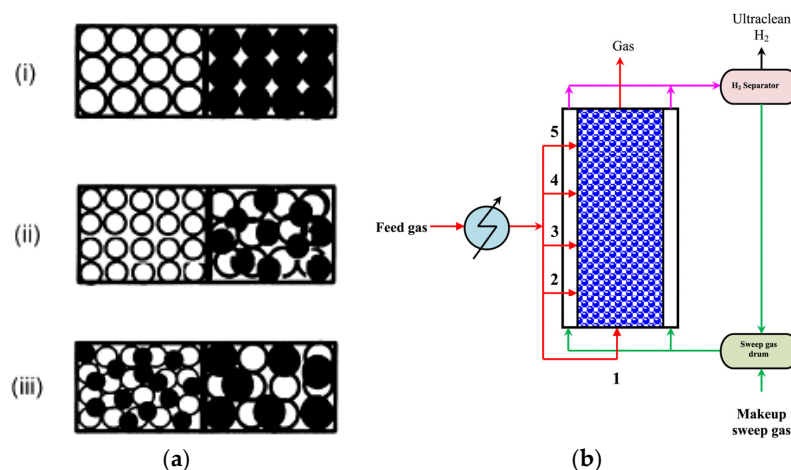

Figure 17. Two types of membrane reactor structures: (**a**) structured catalyst bed membrane reactor with different catalyst configurations [53]; (**b**) FBMR with distributed injection feed [61].

6.5. 3D Simulation in a Membrane Reactor

Most NH_3 decomposition models of membrane reactors are 1D models [56–60] or simplified 2D models [61]. For example, in the 2D model of Abashar et al. [61], they assumed that the reactor and catalyst particles were in isothermal condition and axial diffusion was ignored, which was inconsistent with the actual situation. Only Di Carlo et al. [29] built a 3D model to study NH_3 decomposition and hydrogen production processes in membrane reactors. In the modeling process, they took into account both external and internal diffusion and coupled it to the reaction kinetics. The reactor performance was appraised at different operating pressures, temperatures, and flow rates, and it was found that very high NH_3 conversion (close to thermodynamic equilibrium) occurred only at relatively high temperatures (e.g., 550 °C), relatively low pressures and flow rates. Furthermore, at temperatures above 600 °C, the reaction mostly occurred within a very small region near the reactor inlet.

7. Summary

In this paper, the numerical simulations of NH_3 decomposition under different scenarios are reviewed in detail. The effects of reactor structure and operating conditions on the reactor performance of NH_3 are discussed in depth. The following conclusions can be drawn:

(1) Increasing the reactor temperature, reducing the reaction pressure, especially the hydrogen partial pressure, and increasing the W/F can improve the NH_3 conversion, which applies to all four scenarios discussed in this paper;

(2) The kinetic model of the NH_3 decomposition reaction is crucial to the simulation, and the accuracy of simulation results is highly correlated with the applicability of the selected kinetic model;

(3) The microchannel reactor has high heat and mass transfer efficiency, and therefore the maximum temperature difference inside the reactor is very small (e.g., 0.03 K), and the reaction rate is not limited by mass transfer in the microchannel reactor;

(4) In a multifunctional microreactor, a high-thermal-conductivity wall and co-flow configuration are preferred; if high NH_3 conversion is pursued, a low-thermal-conductivity wall and counterflow configuration can be applied;

(5) There is a significant temperature difference along the flow direction in SOFC. Lowering the working potential is conducive to reducing the temperature difference and increasing the average current density and average power density. However, when the working potential is lower than 0.3V, it may lead to lower output power;

(6) In a membrane reactor, the radial diffusion and permeation of H_2 are restricted due to the concentration polarization at the membrane surface; the membrane reactor structure should be tailored to facilitate the H_2 removal in the reaction region to improve NH_3 conversion.

According to the comprehensive review in this paper, the following topics of NH_3 decomposition are worthy of further study:

(1) The kinetics of the NH_3 decomposition reaction deserves further study to achieve more accurate modeling.

(2) Catalysts with high catalytic efficiency, low catalytic temperature, good stability, long service life and low cost are urgently required. Due to the high efficiency of mass and heat transfer in microreactors, improving the performance of catalysts will significantly improve the performance of microreactors.

(3) The thermal gradient in the post microreactor is very large. It is necessary to seek ways to strengthen the heat transfer between posts and gases and reduce the internal temperature difference.

(4) More carbon-free fuels should be applied to the multifunctional microreactor combining NH_3 decomposition and combustion to reduce CO_2 emission.

(5) There is no model for the overall multi-channel microreactor in the literature, which should be developed.

(6) Most models of membrane reactors are 1D and simplified 2D models, which cannot completely predict the behavior of membrane reactors. Accurate 2D and 3D models need to be developed.

Author Contributions: Conceptualization, R.A. and R.L.; formal analysis, G.L.; investigation, R.A. and G.L.; resources, Q.Y. and F.Y.; data curation, R.A. and Y.Z.; writing—original draft preparation, R.A. and R.L.; writing—review and editing, Q.Y. and F.Y.; visualization, Y.Z.; supervision, Q.Y.; project administration, Q.Y. and F.Y.; All authors have read and agreed to the published version of the manuscript.

Data Availability Statement: Not applicable.

References

1. Mukherjee, S.; Devaguptapu, S.V.; Sviripa, A.; Lund, C.R.F.; Wu, G. Low-temperature ammonia decomposition catalysts for hydrogen generation. *Appl. Catal. B Environ.* **2018**, *226*, 162–181. [CrossRef]

2. Makepeace, J.W.; He, T.; Weidenthaler, C.; Jensen, T.R.; Chang, F.; Vegge, T.; Ngene, P.; Kojima, Y.; de Jongh, P.E.; Chen, P.; et al. Reversible ammonia-based and liquid organic hydrogen carriers for high-density hydrogen storage: Recent progress. *Int. J. Hydrogen Energy* **2019**, *44*, 7746–7767. [CrossRef]

3. Klerke, A.; Christensen, C.H.; Nørskov, J.K.; Vegge, T. Ammonia for hydrogen storage: Challenges and opportunities. *J. Mater. Chem* **2008**, *18*, 2285–2392. [CrossRef]

4. Chein, R.-Y.; Chen, Y.-C.; Chang, C.-S.; Chung, J.N. Numerical modeling of hydrogen production from ammonia decomposition for fuel cell applications. *Int. J. Hydrogen Energy* **2010**, *35*, 589–597. [CrossRef]

5. Waghode, A.N.; Hanspal, N.S.; Shigidi, I.M.T.A.; Nassehi, V.; Hellgardt, K. Computer modelling and numerical analysis of hydrodynamics and heat transfer in non-porous catalytic reactor for the decomposition of ammonia. *Chem. Eng. Sci* **2005**, *60*, 5862–5877. [CrossRef]

6. Chiuta, S.; Everson, R.C.; Neomagus, H.W.J.P.; Bessarabov, D.G. Hydrogen production from ammonia decomposition over a commercial Ru/Al2O3 catalyst in a microchannel reactor: Experimental validation and CFD simulation. *Int. J. Hydrogen Energy* **2016**, *41*, 3774–3785. [CrossRef]

7. Papadiasa, D.; Zwinkels, M.F.M.; Edsberg, L.; BjoÈrnbom, P. Modeling of high-temperature catalytic combustors: Comparison between theory and experimentaldata. *Catal. Today* **1999**, *47*, 315–319. [CrossRef]

8. Hossain, M.K.; Chanda, R.; El-Denglawey, A.; Emrose, T.; Rahman, M.T.; Biswas, M.C.; Hashizume, K. Recent progress in barium zirconate proton conductors for electrochemical hydrogen device applications: A review. *Ceram. Int* **2021**, *47*, 23725–23748. [CrossRef]

9. Hossain, M.K.; Hasan, S.M.K.; Hossain, M.I.; Das, R.C.; Bencherif, H.; Rubel, M.H.K.; Rahman, F.; Emrose, T.; Hashizume, K. A Review of Applications, Prospects, and Challenges of Proton-Conducting Zirconates in Electrochemical Hydrogen Devices. *Nanomaterials* **2022**, *12*, 3581. [CrossRef]

10. Hossain, M.K.; Raihan, G.A.; Akbar, A.; Rubel, M.H.K.; Ahmed, M.H.; Khan, I.; Hossain, S.; Sen, S.K.; Jalal, M.I.E.; El-Denglawey, A. Current Applications and Future Potential of Rare Earth Oxides in Sustainable Nuclear, Radiation, and Energy Devices: A Review. *ACS Appl. Electron. Mater.* **2022**, *4*, 3327–3353. [CrossRef]

11. Lamb, K.E.; Dolan, M.D.; Kennedy, D.F. Ammonia for hydrogen storage; A review of catalytic ammonia decomposition and hydrogen separation and purification. *Int. J. Hydrogen Energy* **2019**, *44*, 3580–3593. [CrossRef]

12. Chen, C.; Wu, K.; Ren, H.; Zhou, C.; Luo, Y.; Lin, L.; Au, C.; Jiang, L. Ru-Based Catalysts for Ammonia Decomposition: A Mini-Review. *Energy Fuels* **2021**, *35*, 11693–11706. [CrossRef]

13. Lucentini, I.; Garcia, X.; Vendrell, X.; Llorca, J. Review of the Decomposition of Ammonia to Generate Hydrogen. *Ind. Eng. Chem. Res.* **2021**, *60*, 18560–18611. [CrossRef]

14. Ganley, J.C.; Thomas, F.S.; Seebauer, E.G.; Masel, R.I. A priori catalytic activity correlations the difficult case of hydrogen production from ammonia. *Catal. Lett.* **2004**, *96*, 117–122. [CrossRef]

15. Temkin, M.; Pyzhev, V. Kinetics of the synthesis of ammonia on promoted iron catalysts. *Acta Physicochim.* **1940**, *12*, 217–222.

16. Harrison, R.H.; Kobe, K.A. Thermodynamics of ammonia synthesis and oxidation. *Chem. Eng. Prog.* **1953**, *49*, 349–353.

17. Tamara, K. A "New" General Mechanism of Ammonia Synthesis and Decomposition on Transition Metals. *Acc. Chem. Res.* **1988**, *21*, 88–94. [CrossRef]

18. Ge´rald Dje´ga-Mariadassou, G.; Chae-Ho Shin, C.H.; Bugli, G. Tamaru's model for ammonia decomposition over titanium oxynitride. *J. Mol. Catal. A Chem.* **1999**, *141*, 263–267. [CrossRef]

19. Maleki, H.; Fulton, M.; Bertola, V. Kinetic assessment of H2 production from NH3 decomposition over CoCeAlO catalyst in a microreactor: Experiments and CFD modelling. *Chem. Eng. J.* **2021**, *411*, 128595. [CrossRef]

20. Chen, L.; Kang, Q.; He, Y.-L.; Tao, W.-Q. Pore-scale simulation of coupled multiple physicochemical thermal processes in micro reactor for hydrogen production using lattice Boltzmann method. *Int. J. Hydrogen Energy* **2012**, *37*, 13943–13957. [CrossRef]

21. Deshmukh, S.R.; Mhadeshwar, A.B.; Vlachos, D.G. Microreactor Modeling for Hydrogen Production from Ammonia Decomposition on Ruthenium. *Ind. Eng. Chem. Res.* **2004**, *43*, 2986–2999. [CrossRef]

22. Zade, A.Q.; Renksizbulut, M.; Friedman, J. Ammonia Decomposition for Hydrogen Production in Catalytic Microchannels with Slip/Jump Effects. *J. Appl. Fluid Mech.* **2015**, *8*, 703–712.

23. Jacob, B. *Dynamics of Fluids in Porous Media*; Courier Corporation: Chelmsford, MA, USA, 1988.

24. Reid, R.C.; Prausnitz, J.M.; Poling, B.E. *The Properties of Gases and Liquids*; U.S. Department of Energy Office of Scientific and Technical Information: Oak Ridge, TN, USA, 1987.

25. Bessler, W.G.; Gewies, S.; Vogler, M. A new framework for physically based modeling of solid oxide fuel cells. *Electrochim. Acta* **2007**, *53*, 1782–1800. [CrossRef]

26. Hayes, R.E.; Kolaczkowski, S.T. *Introduction to Catalytic Combustion*; Routledge: London, UK, 2021.

27. Lamb, K.; Hla, S.S.; Dolan, M. Ammonia decomposition kinetics over LiOH-promoted, α-Al2O3-supported Ru catalyst. *Int. J. Hydrogen Energy* **2019**, *44*, 3726–3736. [CrossRef]

28. Chiuta, S.; Everson, R.C.; Neomagus, H.W.J.P.; Le Grange, L.A.; Bessarabov, D.G. A modelling evaluation of an ammonia-fuelled microchannel reformer for hydrogen generation. *Int. J. Hydrogen Energy* **2014**, *39*, 11390–11402. [CrossRef]

29. Di Carlo, A.; Dell'Era, A.; Del Prete, Z. 3D simulation of hydrogen production by ammonia decomposition in a catalytic membrane reactor. *Int. J. Hydrogen Energy* **2011**, *36*, 11815–11824. [CrossRef]

30. Itoh, N.; Oshima, A.; Suga, E.; Sato, T. Kinetic enhancement of ammonia decomposition as a chemical hydrogen carrier in palladium membrane reactor. *Catal. Today* **2014**, *236*, 70–76. [CrossRef]

31. Molaeimanesh, G.R.; Davarani, M.H.S. A pore-scale model for microfibrous ammonia cracking microreactors via lattice Boltzmann method. *Korean J. Chem. Eng.* **2016**, *33*, 1211–1219. [CrossRef]

32. Schumacher, K.; Engelbrecht, N.; Everson, R.C.; Friedl, M.; Bessarabov, D.G. Steady-state and transient modelling of a microchannel reactor for coupled ammonia decomposition and oxidation. *Int. J. Hydrogen Energy* **2019**, *44*, 6415–6426. [CrossRef]

33. Badakhsh, A.; Kwak, Y.; Lee, Y.-J.; Jeong, H.; Kim, Y.; Sohn, H.; Nam, S.W.; Yoon, C.W.; Park, C.W.; Jo, Y.S. A compact catalytic foam reactor for decomposition of ammonia by the Joule-heating mechanism. *Chem. Eng. J.* **2021**, *426*, 130802. [CrossRef]

34. Wang, B.; Kong, H.; Wang, H.; Wang, Y.; Hu, X. Kinetic and thermodynamic analyses of mid/low-temperature ammonia decomposition in solar-driven hydrogen permeation membrane reactor. *Int. J. Hydrogen Energy* **2019**, *44*, 26874–26887. [CrossRef]

35. Regatte, V.R.; Kaisare, N.S. Hydrogen generation in spatially coupled cross-flow microreactors. *Chem. Eng. J.* **2013**, *215–216*, 876–885. [CrossRef]

36. Zanfir, M.; Gavriilidis, A. Catalytic combustion assisted methane steam reforming in a catalytic plate reactor. *Chem. Eng. Sci.* **2003**, *58*, 3947–3960. [CrossRef]

37. Chen, J.; Yan, L.; Song, W.; Xu, D. Operating strategies for thermally coupled combustion-decomposition catalytic microreactors for hydrogen production. *Int. J. Hydrogen Energy* **2016**, *41*, 21532–21547. [CrossRef]

38. Deutschmanna, O.; Maier, L.I.; Riedel, U.; Stroemman, A.H.; Dibble, R.W. Hydrogen assisted catalytic combustion of methane on platinum. *Catal. Today* **2000**, *59*, 141–150. [CrossRef]

39. Karagiannidis, S.; Mantzaras, J.; Bombach, R.; Schenker, S.; Boulouchos, K. Experimental and numerical investigation of the hetero-/homogeneous combustion of lean propane/air mixtures over platinum. *Proc. Combust. Inst.* **2009**, *32*, 1947–1955. [CrossRef]

40. Qin, Z.W.; Lissianski, V.V.; Yang, H.X.; Gardiner, W.C.; Davis, S.G.; Wang, H. Combustion chemistry of propane: A case study of detailed reaction mechanism optimization. *Proc. Combust. Inst.* **2000**, *28*, 1663–1669. [CrossRef]

41. Deshmukh, S.R.; Vlachos, D.G. CFD Simulations of Coupled, Countercurrent Combustor/Reformer Microdevices for Hydrogen Production. *Ind. Eng. Chem. Res.* **2005**, *44*, 4982–4992. [CrossRef]

42. Jejurkar, S.Y.; Mishra, D.P. Thermal performance characteristics of a microcombustor for heating and propulsion. *Appl. Therm. Eng.* **2011**, *31*, 521–527. [CrossRef]

43. Kaisare, N.S.; Stefanidis, G.D.; Vlachos, D.G. Millisecond Production of Hydrogen from Alternative, High Hydrogen Density Fuels in a Cocurrent Multifunctional Microreactor. *Ind. Eng. Chem. Res.* **2009**, *48*, 1749–1760. [CrossRef]

44. Deshmukh, S.R.; Vlachos, D.G. Effect of flow configuration on the operation of coupled combustor/reformer microdevices for hydrogen production. *Chem. Eng. Sci.* **2005**, *60*, 5718–5728. [CrossRef]

45. Ni, M.; Leung, D.Y.C.; Leung, M.K.H. An improved electrochemical model for the NH3 fed proton conducting solid oxide fuel cells at intermediate temperatures. *J. Power Sources* **2008**, *185*, 233–240. [CrossRef]

46. Ni, M. Thermo-electrochemical modeling of ammonia-fueled solid oxide fuel cells considering ammonia thermal decomposition in the anode. *Int. J. Hydrogen Energy* **2011**, *36*, 3153–3166. [CrossRef]

47. Chan, S.H.; Khor, K.A.; Xia, Z.T. A complete polarization model of a solid oxide fuel cell and its sensitivity to the change of cell component thickness. *J. Power Sources* **2001**, *93*, 130–140. [CrossRef]

48. Ni, M.; Leung, M.K.H.; Leung, D.Y.C. Parametric study of solid oxide fuel cell performance. *Energy Convers. Manag.* **2007**, *48*, 1525–1535. [CrossRef]

49. Ni, M.; Leung, D.Y.C.; Leung, M.K.H. Mathematical modeling of ammonia-fed solid oxide fuel cells with different electrolytes. *Int. J. Hydrogen Energy* **2008**, *33*, 5765–5772. [CrossRef]

50. Chase, M.W. *NIST-JANAF Thermochemical Tables*, 4th ed.; American Institute of Physics: College Park, MD, USA, 1998.

51. Lin, Y.; Ran, R.; Guo, Y.; Zhou, W.; Cai, R.; Wang, J.; Shao, Z. Proton-conducting fuel cells operating on hydrogen, ammonia and hydrazine at intermediate temperatures. *Int. J. Hydrogen Energy* **2010**, *35*, 2637–2642. [CrossRef]

52. Ji, G.Z.; Yao, J.G.; Clough, P.T.; Diniz da Costa, J.C.; Anthony, E.J.; Fennell, P.S.; Wang, W.; Zhao, M. Enhanced hydrogen production from thermochemical processes—a review. *Energy Environ. Sci.* **2018**, *11*, 2647–2672. [CrossRef]

53. Abashar, M.E.E.; Al-Sughair, Y.S.; Al-MutazI, S. Investigation of low temperature decomposition of ammonia using spatially patterned catalytic membrane reactors. *Appl. Catal. A Gen.* **2002**, *236*, 35–53. [CrossRef]

54. Hurlburt, R.C.; Konency, J.O. Diffusion of hydrogen through palladium. *J. Chem. Phys.* **1961**, *34*, 655–658. [CrossRef]

55. Ackerman, F.J.; Koskinas, G.J. Permeation of Hydrogen and Deuterium Through Palladium-silver Alloys. *J. Chem. Eng.* **1972**, *17*, 51–55. [CrossRef]

56. Rahimpour, M.R.; Mottaghi, H.R.; Barmaki, M.M. Hydrogen production from urea wastewater using a combination of urea thermal hydrolyser–desorber loop and a hydrogen-permselective membrane reactor. *Fuel Process. Technol.* **2010**, *91*, 600–612. [CrossRef]

57. Rahimpour, M.R.; Asgari, A. Modeling and simulation of ammonia removal from purge gases of ammonia plants using a catalytic Pd-Ag membrane reactor. *J. Hazard Mater.* **2008**, *153*, 557–565. [CrossRef] [PubMed]

58. Israni, S.H.; Nair, B.K.R.; Harold, M.P. Hydrogen generation and purification in a composite Pd hollow fiber membrane reactor: Experiments and modeling. *Catal. Today* **2009**, *139*, 299–311. [CrossRef]

59. Li, G.; Kanezashi, M.; Yoshioka, T.; Tsuru, T. Ammonia decomposition in catalytic membrane reactors: Simulation and experimental studies. *AIChE J.* **2013**, *59*, 168–179. [CrossRef]

60. Zhang, Z.; Liguori, S.; Fuerst, T.F.; Way, J.D.; Wolden, C.A. Efficient Ammonia Decomposition in a Catalytic Membrane Reactor To Enable Hydrogen Storage and Utilization. *ACS Sustain. Chem. Eng.* **2019**, *7*, 5975–5985. [CrossRef]

61. Abashar, M.E.E. The impact of ammonia feed distribution on the performance of a fixed bed membrane reactor for ammonia decomposition to ultra-pure hydrogen. *Int. J. Hydrogen Energy* **2019**, *44*, 82–90. [CrossRef]